Editors' Suggestion

Liquid spreading along nanostructured superhydrophilic lanes

Seungho Kim,[1] Myoung-Woon Moon,[2] and Ho-Young Kim[1,*]
[1]*Department of Mechanical Engineering, Seoul National University, Seoul 08826, Korea*
[2]*Extreme Materials Research Center, Korea Institute of Science and Technology, Seoul 02792, Korea*

(Received 1 November 2020; accepted 11 February 2021; published 8 March 2021)

A liquid hanging from a liquid-filled tube can spread spontaneously on rough hydrophilic surfaces while it cannot on smooth hydrophilic surfaces, a difference resulting from the competition between the capillary suction pressures provided by the tube and by the surface roughness. In order to pattern liquids on solid surfaces utilizing such wetting characteristics, we investigate the dynamics of a spontaneous liquid spreading from a tube onto a nanostructured superhydrophilic microlane surrounded by a superhydrophobic background. We find distinct regimes of liquid film propagation dynamics to arise depending on the lane width and the liquid column height in the tube. We theoretically analyze the spreading rates of films, which change power laws in the course of spreading, and corroborate the theory with experiments. The spontaneous liquid patterning process reported in this work can provide a viable venue for such applications as electronic circuit printing and biochip fabrication.

DOI: 10.1103/PhysRevFluids.6.034002

I. INTRODUCTION

Spreading of liquids on micro- or nanotextured solid surfaces has been the subject of intense study owing to the development of various surface micromachining processes. The wettability of solid surfaces tends to be magnified as they are roughened, so that rough hydrophilic surfaces turn superhydrophilic. The most salient feature of spreading on textured superhydrophilic surfaces is that the liquid film tends to wick through the gaps of surface protrusions. Such film flow driven by the high surface energy of the rough surfaces is termed hemiwicking [1,2], which exhibits rich spreading behaviors as exemplified in the following. Small drops deposited on hydrophilic arrays of micropillars form polygons rather than circular lenses by filling the gaps of the pillar array through zippering [3]. When a vertical superhydrophilic plate touches a liquid pool, the liquid meniscus climbs a great distance against gravity [2]. The ability to write with a pen (or capillary tube) on porous paper (or micropillar array) using ink is owing to the roughness of the solid surface [4], without which the liquid hardly spreads out from a pen onto the surface.

The enhanced wettability of textured surfaces can be used to pattern liquid deposits into various two-dimensional shapes, which may find diverse applications in electronic circuit printing [5], biochip fabrication [6,7], and water harvesting from humid air or fog [8–10]. Using wettable islands surrounded by a nonwetting background, Namib Desert beetles [8] and cribellate spiders [10] have been reported, respectively, to facilitate drainage of water drops from their backs to mouths and to prevent water loss by the wind. Predefined superhydrophilic patterns surrounded by a hydrophobic background allow us to achieve rapid liquid sculpture. It has been shown earlier that liquids can advance along smooth hydrophilic strips under the thermal Marangoni stress [11,12]. Retraction of liquid deposits can also lead to liquid patterns. As the initially circular liquid deposit recedes by

*hyk@snu.ac.kr

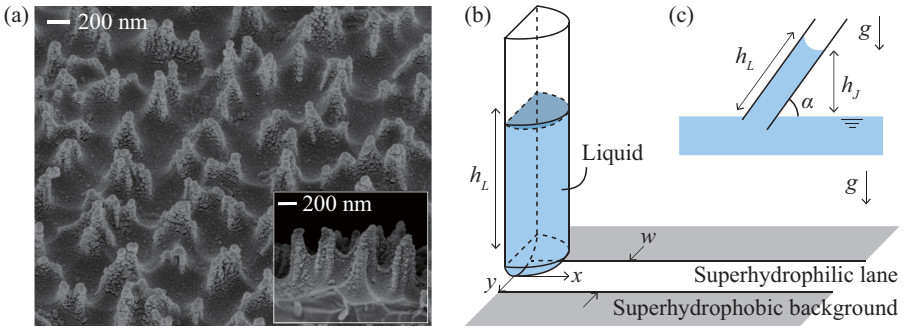

FIG. 1. (a) Scanning electron microscopy image of nanograsses formed on a Si wafer. The inset shows a side view of the nanograsses. (b) A schematic of a capillary tube with a hanging drop that touches a superhydrophilic microlane of the width w. The initial height of the liquid column in the tube is denoted by h_L. (c) A tilted tube to imbibe liquid more than Jurin's height h_J.

either oscillation [13] or evaporation [14], the liquid is arrested on the hydrophilic pattern while being removed from the hydrophobic region.

Directional spreading of a liquid deposit has been demonstrated on a surface with tilted microtextures specially prepared to allow the liquid to flow in one direction [15]. By designing the spatial distribution of directed microstructures, one can pattern liquids in the desired shape [16]. However, the considerable time and cost for the fabrication of directional microstructures may hinder the wide application of the liquid patterning scheme.

Here we show that liquids can spontaneously spread along predefined rough hydrophilic lanes, which can be fabricated through a relatively low-cost process on a large area. The spontaneous advancing of liquid over a dry surface is due to the extreme wettability of the surfaces arising from the surface texture that increases the area of high surface energy. We find that liquid films of drastically different thicknesses can be obtained by merely adjusting the lane width. Furthermore, the propagation dynamics of the liquid film undergo multiple regime changes, so that the power law of the wetting distance versus time changes in the course of spreading.

In the following, we start with a description of the experimental procedures and representative observation results. We then theoretically analyze the rich dynamics of film propagation along the superhydrophilic lane, which are dependent on the lane width and static pressure at the starting point as well as the liquid properties and surface roughness. Our theory is corroborated by the experimental measurements.

II. EXPERIMENTAL

A. Experimental procedures

To create a superhydrophilic microlane surrounded by a superhydrophobic background on a Si wafer, we cleaned the wafer with Ar gas and formed nanoscale roughness on the surface using the CF_4 etching in a plasma-assisted chemical vapor deposition (PACVD) chamber for 50 min. Then, an amorphous $C_6H_{18}Si_2O$ layer was deposited on the surface using hexamethyldisiloxane gas in the PACVD process, which lowered the surface energy [17]. The resulting surface was covered with superhydrophobic nanograsses as shown in Fig. 1(a). The average values ($\pm$ standard deviation) of the diameter d, the height h_p, and the center-to-center spacing s of ten typical nanoprotrusions were measured to be 146 ± 25, 560 ± 74, and 467 ± 91 nm, respectively.

Assuming the rough surface as a square array of cylindrical pillars, the measured average dimensions of the protrusions allow us to estimate the surface roughness f, the ratio of the actual surface area to the projected area, as $f = 1 + \pi d h_p / s^2 = 2.2$. We also measured the roughness using an atomic force microscope (AFM; Park Systems XE-70) by scanning three different areas of

TABLE I. Liquid properties at 23 °C.

	Liquid	ρ (kg/m^3)	γ (N/m)	μ (Pa s)
A	Water	998	0.072	0.001
B	Glycerine 60 wt%	1151	0.067	0.009
C	Ethanol	789	0.022	0.0014

$10 \times 10\ \mu m^2$ to find $f = 1.9 \pm 0.2$. The measured roughness is approximately 14% lower than the calculated value, which is supposed to be caused in part by the tip convolution effects of AFM [18] as well as our simplified assumption of the surface topography. In our theoretical modeling given below, we use the experimentally measured value of $f = 1.9$ when necessary.

We selectively covered the superhydrophobic area with a photoresist except for a microlane via the photolithography process. The uncovered microlane was treated with air plasma to turn superhydrophilic owing to the raised surface energy. Removal of the residual photoresist with acetone resulted in a surface with a superhydrophilic microlane surrounded by a superhydrophobic background [14]. The width of the superhydrophilic lane, w, ranged from 0.2 to 4.0 mm. By imaging water drops of 2 μl in volume, the equilibrium contact angle θ_e of the superhydrophobic region was measured to be $160 \pm 2^\circ$.

We used water, aqueous glycerine of 60 wt%, and ethanol as liquids to spread on the microlane, whose density ρ, surface tension coefficient γ, and viscosity μ are listed in Table I. Figure 1(b) shows an experimental setup, where the liquid is supplied from a capillary tube of inner radius $a = 0.58$ mm onto a substrate. The liquid pressure at the starting point of the microlane, corresponding to $\rho g h_L$, with g being the gravitational acceleration, was varied by changing the initial height of the liquid column in the tube, h_L. To this end, we first cleaned the capillary tube with piranha solution, which made the inner surface of tube highly wettable. We brought the tube in contact with the free surface of a liquid pool to induce capillary rise of the liquid against gravity. The equilibrium rise height, referred to as Jurin's height [19], is given by $h_J = 2\gamma/(\rho g a)$. The initial liquid column height could be varied by either dislodging the tube from the liquid free surface before equilibrium was reached ($h_L < h_J$) or tilting the tube at an angle α until the vertical rise height reached equilibrium ($h_L = h_J/\sin\alpha \geqslant h_J$) as shown in Fig. 1(c). If $h_L > h_J$, an excessive hydrostatic pressure at the bottom of the vertically situated tube, $\rho g(h_L - h_J)$, led to a drop hanging underneath the tube, which could spontaneously spread along the microlane when in contact with the solid surface. If $h_L < h_J$, the liquid meniscus at the bottom of the tube was formed inward because the liquid pressure was lower than the atmospheric pressure. However, contacting the tube end with the rough solid surface caused the inward meniscus to touch the superhydrophilic nanograsses, resulting in wicking of the liquid onto the microlane. The liquid spreading dynamics were imaged by a complementary metal-oxide-semiconductor camera (Photron Fastcam SA1.1) at a frame rate of 1000 s^{-1}.

B. Observations

A liquid that emanates from the tube end can propagate only along the superhydrophilic lane without invading the superhydrophobic region. Figures 2(a) and 2(b) show our imaging results of water films that spread on the hydrophilic microlanes of different widths (see also Videos S1 and S2 of Supplemental Material [20]). Despite the identical hydrostatic pressure exerted at the bottom of the tube for the same initial liquid column height ($h_L = 38$ mm), a drastic difference in the spreading behaviors is observed between the narrow lane of $w = 0.2$ mm [Fig. 2(a)] and the wide lane of $w = 0.6$ mm [Fig. 2(b)]. For the narrow lane, a fairly thin film is entrained along the lane, with the wetting front appearing smooth at the macroscopic scale but zigzag at the microscopic scale [inset in the panel at time $t = 33$ ms in Fig. 2(a)]. Such a thin film that wicks into the gaps of nanograsses is herein referred to as the fringe film, whose thickness is defined by the nanograss

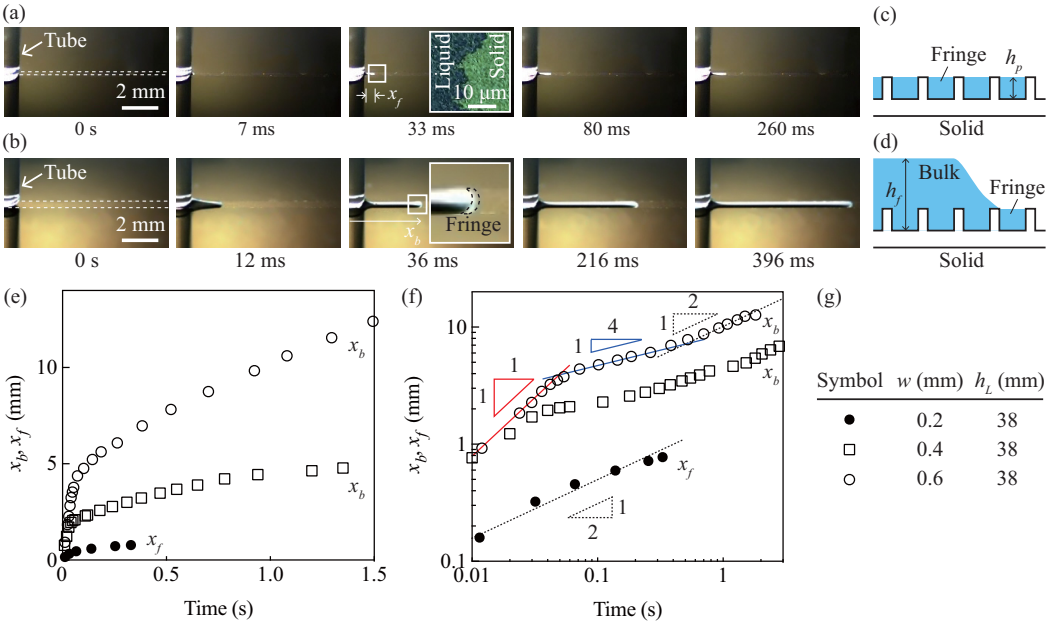

FIG. 2. Spreading of water films from a tube (loaded with the same height of the liquid column, $h_L = 38$ mm) onto superhydrophilic microlanes of different widths. The lane widths are (a) $w = 0.2$ mm and (b) $w = 0.6$ mm. Insets in panels (a) and (b) respectively show the magnified views of the zigzag front of the fringe film and of the fringe film preceding the bulk. (c) A schematic of the longitudinal cross section of the fringe film on the narrow lane. (d) A schematic of the longitudinal cross section of the bulk film on the wide lane. (e) Experimentally measured spreading distances of the fringe film (x_f) and the bulk film (x_b) versus time. (f) The log-log plot of the spreading distances versus time. (g) Experimental conditions for the symbols.

height h_p [2,21] as illustrated in Fig. 2(c). For the wide lane, a relatively thick film, referred to as a bulk film, spreads along the lane with its advancing front preceded by a short fringe film as imaged in the inset of the panel at $t = 36$ ms in Fig. 2(b) and illustrated in Fig. 2(d). Although the fringe film arises in both the narrow and the wide lane, the bulk emerges only on the wide lane.

Figure 2(e) shows the representative measurement results of the spreading distance of the fringe film on the narrow lane (x_f) and the bulk films in the wide lanes (x_b). We see that the bulk films spread considerably faster than the fringe film and that the bulk film on a wider lane ($w = 0.6$ mm) propagates faster than that on a narrower lane ($w = 0.4$ mm). The log-log plot in Fig. 2(f) reveals that the bulk spreading dynamics undergo three regimes with different power laws of $x_b \sim t^n$, where n changes as 1, 1/4, and 1/2 as time elapses. The fringe film grows like $t^{1/2}$ all the time. In the following, we theoretically analyze the dynamics of the fringe and bulk films as well as the transition condition from the fringe film to the bulk film.

III. THEORETICAL ANALYSIS

A. Spreading of fringe films

Figure 3(a) shows the emergence and temporal evolution of a fringe film on a lane 2 mm in width (see Video S3 of Supplemental Material [20]). When the drop hanging from the tube touches the substrate at $t = 0$, the bulk meniscus forms but stops spreading at $t = 4$ ms. This is because the hydrostatic pressure $\rho g(h_L - h_J)$ is not strong enough to overcome the capillary pressure formed by the curved bulk meniscus as is delineated in Sec. III B. Since then the fringe film propagates along the lane, whose extension is measured from the edge of the bulk as x_f. The measurement results of

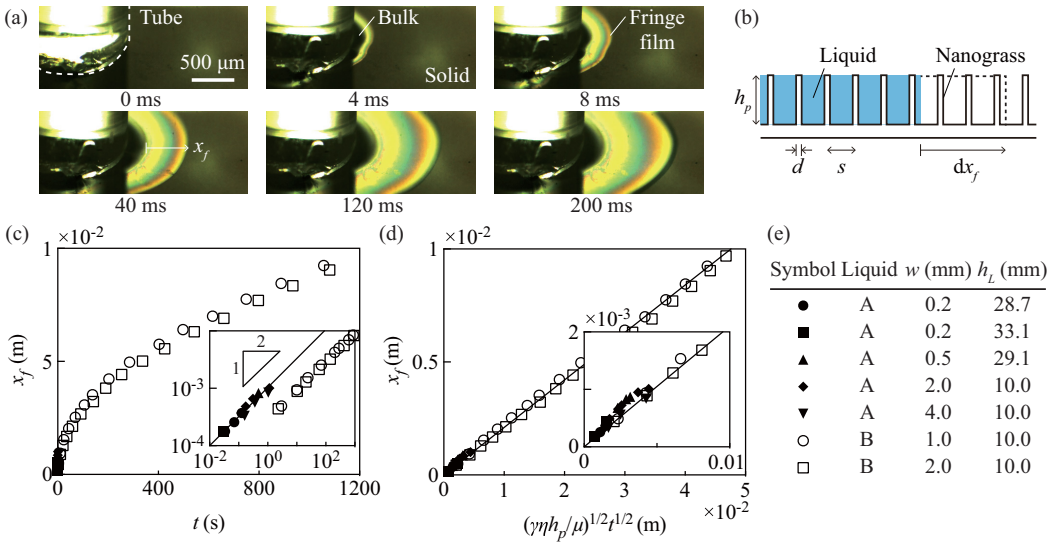

FIG. 3. (a) Sequential images of a propagating fringe film of water emerging from a bulk beneath a capillary tube when $[w, h_L] = [2, 10]$ mm. (b) Schematic of the cross-sectional view of the wetted nanograsses. (c) Measurement results of x_f versus time for different liquids, lane widths, and initial liquid column heights. Inset: The log-log plot of the main graph. (d) The fringe extension x_f plotted according to scaling law (1). The slope of the best fitting line is 0.21. Inset: The magnified plot for the initial time period. (e) Experimental conditions for the symbols.

x_f, displayed in Fig. 3(c), indicate that x_f is sensitive to the liquid properties but independent of the lane width and the hydrostatic pressure.

Although the bulk cannot grow as blocked by the capillary pressure, the fringe film can wick into the gaps of nanograsses as driven by the high surface energy of the solid. Here we employ a theoretical model of Kim *et al.* [2], which was validated for hemiwicking in regular arrays of microscale cylindrical pillars, to predict the velocity of the current nanoscale wicking flow. Because the flow emerges from the circular tube-substrate contact area, the fringe front appears curved especially when the lane width is greater than 2 mm. However, here we employ the two-dimensional wicking model because the flow is dominantly guided along the lane's longitudinal direction and the tube's outer diameter (1.6 mm) is greater than or comparable to the widths of our lanes.

As the fringe film extends from x_f to $x_f + \mathrm{d}x_f$ as shown in Fig. 3(b), the surface energy increases by $dE = [\gamma(1-\phi) + (\gamma_{SL} - \gamma_{SG})(f-\phi)]w dx_f$, where γ_{SL} and γ_{SG} respectively denote the solid-liquid and solid-gas interfacial energy per unit area, and ϕ is the area fraction of the top of protrusions not wetted by the liquid film ($\phi \approx 0.08$). The first term in the right-hand side corresponds to the energy increase of the liquid-gas interface and the second term to the energy increase associated with the wetting of initially dry solid surface. As $\gamma_{SG} - \gamma_{SL} \approx \gamma$ via Young's equation for a highly wettable solid surface, we get the driving force of film spreading $F_d = -dE/dx_f = \gamma(f-1)w$, which states that the rougher the surface is (higher f), the stronger the driving force is.

The viscous resisting force F_r comes from shear stresses at the bottom area and the side walls of the protrusions; it was shown to be scaled as [2] $F_r \sim \mu x_f \dot{x}_f [1/h_p + (f-1)/s]$, with $\dot{x}_f = dx_f/dt$. Balancing F_d and F_r gives the spreading speed of the inertialess fringe film flow: $\dot{x}_f \sim \gamma\eta h_p/(\mu x_f)$, with $\eta = (f-1)/[1 + h_p(f-1)/s]$. Integration yields the following diffusive behavior of the

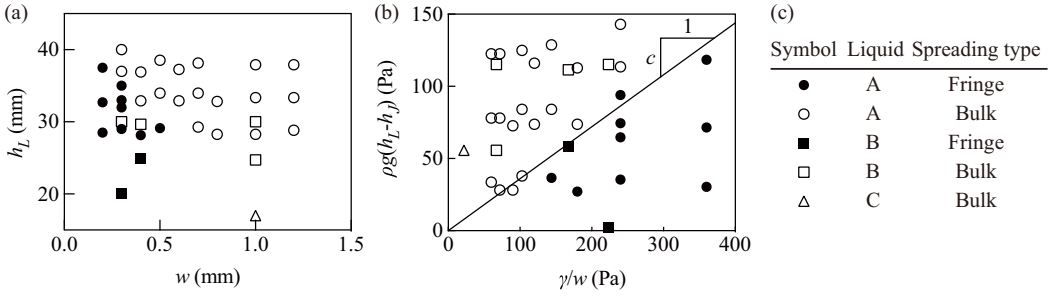

FIG. 4. (a) Types of liquid spreading depending on the width of the lane, w, and the height of the liquid column, h_L. The solid and empty symbols correspond to the fringe and the bulk spreading, respectively. (b) Experimental data in panel (a) are replotted according to scaling law (2). The slope of the best fitting line, c, is 0.36. (c) Experimental conditions for the symbols.

wicking distance:

$$x_f \sim \left(\frac{\gamma}{\mu}\eta h_p\right)^{1/2} t^{1/2}. \tag{1}$$

We plot the measurement data of x_f according to scaling law (1) in Fig. 3(d) to see that the data for different liquids A and B are collapsed onto a single line. The results indicate that the hemiwicking model based on the balance of the capillary driving force and the viscous resisting force holds for our fringe films in the gaps of nanograsses with diameter, height, and spacing on the order of 100 nm.

B. Transition from fringe to bulk spreading

It is our experimental observation that the bulk can spread along the superhydrophilic lane as the initial liquid column height and the lane width increase. This naturally leads us to suppose that the transition from the fringe to bulk spreading is associated with the balance between the hydrostatic pressure and the capillary pressure, which respectively drives and resists the bulk flow. The hydrostatic pressure at the tube bottom is given by $\rho g(h_L - h_J)$. The bulk can emanate from the tube when this pressure overcomes the capillary pressure that corresponds to a product of the surface tension coefficient and the meniscus curvature (κ) determined by the lane width, $\kappa \sim 1/w$. The pressure balance allows us to predict the regime boundary between fringe and bulk spreading as

$$\rho g(h_L - h_J) \sim \frac{\gamma}{w}. \tag{2}$$

Figure 4(a) displays the experimentally obtained flow type in the two-dimensional parameter space constructed with h_L and w—the solid and the empty symbols correspond to the fringe and the bulk film, respectively. Plotting the data according to scaling law (2) in Fig. 4(b), we see that the two flow regimes are divided by a single line indicating $\rho g(h_L - h_J) = c\gamma/w$. Here the empirical prefactor c is found to be 0.36. Only fringe films can spread along the lanes when $w(h_L - h_J) < cl_c^2$, and the bulk film can spread as either w or h_L increases to fulfill $w(h_L - h_J) > cl_c^2$, with the capillary length l_c defined as $l_c = [\gamma/(\rho g)]^{1/2}$.

C. Spreading of bulk films

1. Early stages

We start with the early stages of bulk spreading, where x_b grows like t, as is shown in Fig. 2(f) (see Video S4 of Supplemental Material [20]). As soon as the drop hanging from the capillary tube

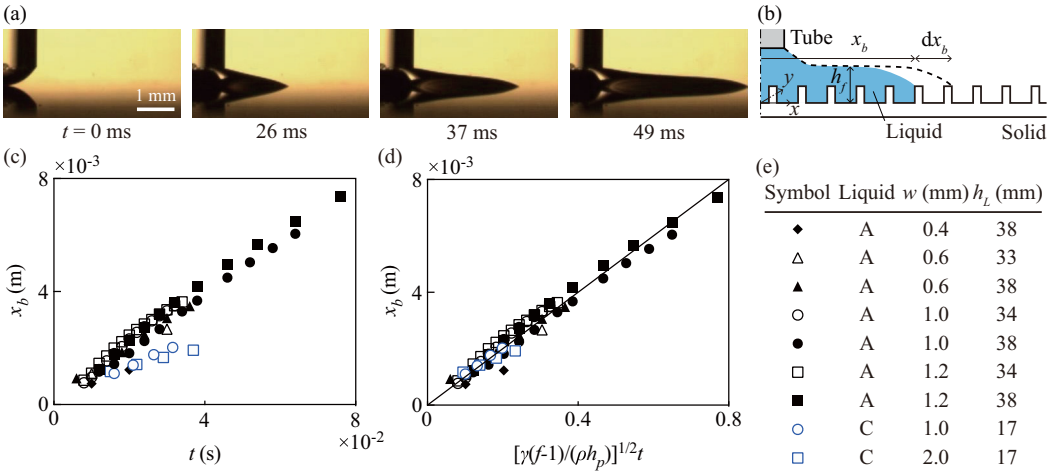

FIG. 5. (a) Images of a propagating bulk water film in the early stages for $[w, h_L] = [1.0, 38]$ mm. (b) Schematic of bulk spreading in the early stages. (c) Experimentally measured temporal evolution of bulk film, x_b, under different experimental conditions. (d) The experimental data of x_b plotted according to scaling law (3). (e) Experimental conditions for the symbols.

touches the superhydrophilic surface, it rapidly spreads along the lane as imaged in Fig. 5(a). To understand the major forces that work in determining the bulk propagation dynamics, we compare the viscous and inertial forces. We consider a two-dimensional flow which is guided along the lane's longitudinal direction because the bulk extension is much greater than the lane width for most of the cases shown in Fig. 5, and the tube's outer diameter is greater than or comparable to the widths of our lanes.

As the bulk film effectively slips at the bottom owing to rapid wicking in the superhydrophilic nanograsses, the characteristic velocity gradient in the bulk is of order $\dot{x}_b/x_b$ [21,22], allowing us to estimate the viscous force as $\sim\mu\dot{x}_b w$. Then the ratio of inertial to viscous force is given by the Reynolds number, $\mathrm{Re} = \rho\dot{x}_b h_f/\mu$. We neglect the viscous effects in this initial period for $\mathrm{Re} \gg 1$. Then the x-directional Euler equation leads us to balance the pressure difference driving the initial bulk spreading, Δp, with the dynamic pressure that resists the flow, $\sim\rho\dot{x}_b^2$.

The driving pressure comes from the hydrostatic contribution of the liquid column, $\Delta p_g = \rho g(h_L - h_J)$, and the capillary pressure originated by the high surface energy of the hydrophilic rough surface. The capillary pressure is given by $\Delta p_c = F_c/(wh_p)$, where the capillary force F_c is obtained using the energy change dE_c associated with the spreading of bulk by a distance dx_b as illustrated in Fig. 5(b). As the bulk film entirely covers the hydrophilic nanograsses, we get $dE_c = [\gamma + f(\gamma_{SL} - \gamma_{SG})]wdx_b = -\gamma(f-1)wdx_b$. Then the capillary force $F_c = -dE_c/dx_b$ leads to $\Delta p_c \sim \gamma(f-1)/h_p$. As Δp_c dominates over Δp_g for $\Delta p_c/\Delta p_g \sim 10^3 - 10^4$ in our experiments, we balance Δp_c with $\rho\dot{x}_b^2$, which reveals that the bulk film spreads with a constant velocity. Thus, we obtain the following scaling law for the extension of the bulk film in the early stages:

$$x_b \sim \left[\frac{\gamma(f-1)}{\rho h_p}\right]^{1/2} t. \tag{3}$$

We see that the spreading rate is dependent on the liquid properties (γ and ρ) and surface topography (f and h_p) but independent of the lane width (w) and the liquid column height (h_L).

Figure 5(c) shows the experimental measurement results of the bulk spreading distance x_b versus time for different liquids, w and h_L. The data for water (liquid A) indeed exhibit an almost identical slope (velocity) regardless of w and h_L, while those of liquid C have a slope for its lower surface

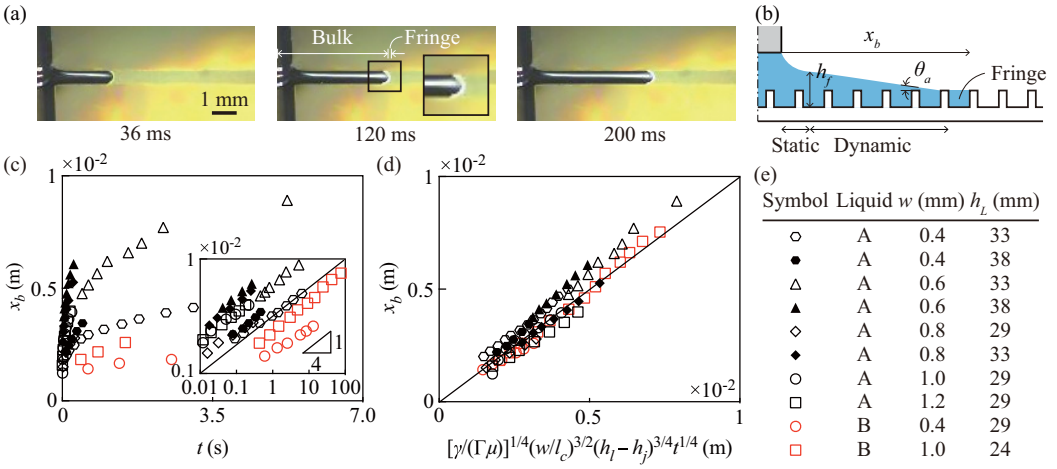

FIG. 6. (a) Sequential images of a propagating bulk film of water in the middle stages for $[w, h_L] = [0.8, 33]$ mm. (b) A schematic of bulk spreading in the middle stages. (c) Experimentally measured temporal evolution of the bulk film extension, x_b, under different experimental conditions. Inset: The log-log plot of x_b versus t. (d) The experimental data of x_b plotted according to scaling law (4). The slope of the best fitting line is 1.0. (e) Experimental conditions for the symbols.

tension coefficient smaller than that for liquid A. Plotting the raw data according to our scaling law (3) in Fig. 5(d), we find the data for liquid C to collapse onto the same line as liquid A.

2. Middle stages

Beyond the early stages, viscous dissipation slows down the spreading bulk, which leads to the detectable emergence of a fringe film ahead of the bulk, as can be seen in Fig. 6(a) (see Video S5 of Supplemental Material [20]). This observation is consistent with the previously reported, delayed emergence of visible fringe film in front of a bulk that rises through a rough hydrophilic channel [23]. The middle stages of bulk spreading, characterized by the reduced speed of bulk and the visible fringe film, imply the change of forces that dominate the bulk dynamics.

The bulk lying on a prewetted film, schematically shown in Fig. 6(b), is driven to spread by the uncompensated Young force, $F_d = \gamma(1 - \cos\theta_a)w$ [21]. Namely, the curved meniscus with a front angle of θ_a tends to flatten out in order to achieve an even smaller equilibrium contact angle. The advancing contact angle of the bulk on the fringe film, θ_a, can be estimated as $\theta_a \sim x_b/h_f$, where h_f is the characteristic height of the bulk as is modeled below. For small θ_a, we approximate $F_d \sim \gamma\theta_a^2 w$ for $1 - \cos\theta \approx \theta^2/2$.

The resisting force is dominantly given by the viscous effects because $\mathrm{Re} \sim 10^{-1}$ in these stages. The viscous forces arise in both the bulk and the wedge regions, which are away from and adjacent to the contact line, respectively. The bulk resisting force due to the wall shear stress, $\tau \sim \mu\dot{x}_b/h_f$, is estimated as $F_b \sim \mu\dot{x}_b x_b w/h_f$. Near the contact line where the film height is written as $h(\xi) \approx \xi\theta_a$, where ξ is the horizontal distance from the contact line, integration of the wall shear stress, $\tau \sim \mu\dot{x}_b/h(\xi)$, from $\xi = \lambda$ to $\xi = \Lambda$ gives the wedge resisting force $F_w \sim \mu\dot{x}_b\Gamma w/\theta_a$. Here, λ is a cutoff length introduced instead of zero to prevent the integral from tending to infinity (or contact line singularity), Λ is the characteristic extension of the wedge, and $\Gamma = \ln(\Lambda/\lambda)$. By taking $\lambda = h_p$ and $\Lambda = h_f$, we get $\Gamma = \ln(h_p/h_f)$, whose magnitude is estimated as $\Gamma \sim 10$. The wedge resisting force dominates over the bulk resisting force, or $F_b/F_w \ll 1$, when $x_b \ll 10^{-2}$ m. Balancing F_d and F_w leads us to write $\dot{x}_b \sim \gamma h_f^3/(\mu\Gamma x_b^3)$.

Now we are to express the characteristic film thickness h_f as a function of the given parameters. We adopt an approach similar to the model predicting the liquid meniscus profile on a solid surface

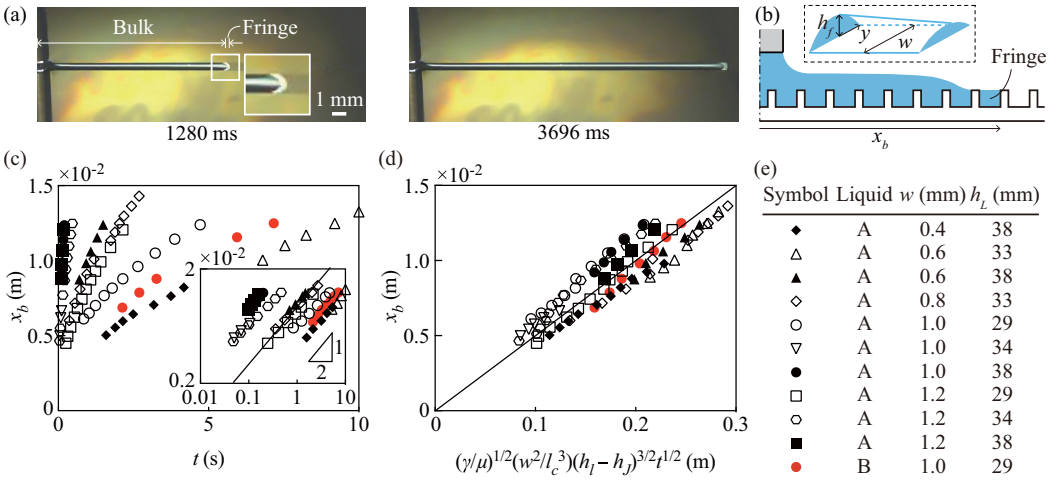

FIG. 7. (a) Sequential images of a propagating bulk film of water in the late stages for $[w, h_L] = [0.8, 33]$ mm. (b) A schematic of bulk spreading in the late stages. The inset shows the cross-sectional shape change of the bulk along the longitudinal direction, where the central thickness of the bulk, h_f, decreases with x. (c) Experimentally measured temporal evolution of the bulk film, x_b, under different experimental conditions. Inset: The log-log plot of x_b versus t. (d) The experimental data of x_b plotted according to scaling law (5). (e) Experimental conditions for the symbols.

that is withdrawn from a liquid pool, i.e., the Landau-Levich theory [24,25]. We decompose the liquid meniscus of the bulk into two regions as indicated in Fig. 6(b): a highly curved static region close to the tube and a relatively flat dynamic region away from the tube. Contrast in shades on the top view of the bulk in Fig. 6(a) allows us to clearly distinguish the dark curved static region from the bright flat region. Then the dynamic contact angle θ_a is estimated based on the characteristic bulk height h_f instead of a vertical gap distance between the tube and the substrate. We note that in a different situation where the horizontal extension of the bulk is comparable to the tube-substrate gap distance, as in the second panel of Fig. 5(a), the dynamic contact angle can be estimated based on the ratio of the two lengths [26]. The pressure at the static region is determined by hydrostatics as $\rho g(h_l - h_J)$, with h_l being the instantaneous liquid column height. The pressure in the dynamic region is given by the capillary pressure of the bulk film: $\sim \gamma h_f / w^2$. Balancing the pressures yields $h_f \sim (w/l_c)^2(h_l - h_J)$.

Therefore, the scaling law for x_b in the middle stages is finally obtained as

$$x_b \sim \left(\frac{\gamma}{\mu\Gamma}\right)^{1/4} \left(\frac{w}{l_c}\right)^{3/2} (h_l - h_J)^{3/4} t^{1/4}. \tag{4}$$

Unlike the spreading rate in the early stages, the bulk propagation velocity depends on the lane width w and the liquid column height h_l as well as the liquid properties. Figure 6(c) shows the experimental data of x_b in the middle stages, which exhibit a power-law behavior of $x_b \sim t^{1/4}$ as shown in the inset of Fig. 6(c). We see in Fig. 6(d) that the scattered raw data are collapsed onto a straight line when plotted according to scaling law (4).

3. Late stages

As the bulk further spreads along the superhydrophilic lane, the bulk is so long, as shown in Fig. 7(a) (see Video S6 of Supplemental Material [20]), that the bulk resisting force $F_b \sim \mu \dot{x}_b x_b w / h_f$ overtakes the resisting force arising at the wedge near the advancing front [27]. In addition, the dynamic contact angle has been significantly reduced, implying that the uncompensated Young force

TABLE II. Scales of driving and resisting forces and corresponding power laws in each film flow regime.

Spreading film	Driving force	Resisting force	Power law
Fringe	Hemiwicking, $\sim\gamma(f-1)w$	Viscous force by nanopillars, $\sim\mu x_f\dot{x}_f[1/h_p+(f-1)/s]$	$x_f\sim t^{1/2}$
Bulk (early stages)	Hemiwicking, $\sim[\gamma(f-1)/h_p]wh_f$	Bulk inertia, $\sim\rho\dot{x}_b^2(wh_f)$	$x_b\sim t$
Bulk (middle stages)	Uncompensated Young's force, $\sim\gamma\theta_a^2 w$	Wedge viscous force, $\sim(\mu\dot{x}_b\Gamma/\theta_a)w$	$x_b\sim t^{1/4}$
Bulk (late stages)	Capillary relaxation force, $\sim\gamma h_f^2/w$	Bulk viscous force, $\sim(\mu\dot{x}_b/h_f)wx_b$	$x_b\sim t^{1/2}$

no longer plays an important role. Instead, the flow is driven by the capillary pressure difference between the starting region of the relatively high curvature and the less curved advancing front, as illustrated in Fig. 7(b). Darhuber *et al.* [28] revealed that the height of a long thin strip of liquid driven by the Marangoni stress indeed decreases along the length. Thus, we estimate the change of film meniscus curvature giving rise to the driving capillary effects as $\kappa\sim h_f/w^2$. Multiplying the corresponding capillary pressure $\gamma\kappa$ with the characteristic area wh_f gives an estimate of the driving force, $F_d\sim\gamma h_f^2/w$.

Balancing the driving force F_d and the resisting force F_b gives the spreading rate $\dot{x}_b\sim\gamma h_f^3/(\mu w^2 x_b)$. Noting that $h_f\sim(w/l_c)^2(h_l-h_J)$ as found in the model for the middle stages, we obtain a scaling law for the bulk spreading distance in the late stages:

$$x_b\sim\left(\frac{\gamma}{\mu}\right)^{1/2}\left(\frac{w^2}{l_c^3}\right)(h_l-h_J)^{3/2}t^{1/2}. \tag{5}$$

Figure 7(c) shows that the experimentally measured x_b values in the late stages follow the $t^{1/2}$ law, although they are scattered for different lane widths, liquid column heights, and liquid properties. The raw data are collapsed onto a single line when plotted according to scaling law (5), which validates our theory.

IV. CONCLUSIONS

We have experimentally shown that liquids can spread along predefined rough hydrophilic lanes surrounded by superhydrophobic backgrounds, and we have theoretically analyzed the liquid propagation dynamics. When the hydrostatic pressure at the starting point of the superhydrophilic lane is not strong enough to overcome the capillary pressure owing to the small lane width, only a fringe film wicking through the gaps of the surface protrusions spreads with the distance following $x_f\sim t^{1/2}$. When the hydrostatic pressure is sufficiently strong, the bulk film can propagate along the lane, whose dynamics evolve in such a sequence that $x_b\sim t, t^{1/4}$, and then $t^{1/2}$. Dominant forces that drive and resist the flows in each regime have been identified, and balancing the forces has yielded scaling laws for the distance of film spreading. Table II summarizes the driving and resisting forces, and the resulting power laws corresponding to each flow regime. We can readily predict when the bulk spreading changes its power law from that of the early stages to the middle stages by equating the power laws of those regimes, Eqs. (3) and (4). The same applies to when the power law changes from that of the middle stages to that of the late stages, by equating Eqs. (4) and (5).

Our theory allows us to tune material properties and geometric parameters to enhance the spreading rate of the fringe and bulk films on superhydrophilic lanes. Increasing the surface tension coefficient and the surface roughness amplifies the driving force of hemiwicking and thus enhances the spreading rate of fringe films and bulk films in the early stages. For middle and late stages of

bulk spreading, the increase of liquid density, the lane width, and the liquid column height, as well as the surface tension coefficient, raises the spreading rate of bulk films.

Patterning the wettability of solid surfaces such that predefined areas of high wettability are surrounded by hydrophobic background allows us to form various shapes of liquid deposits following the wettable patterns [13,14,28]. Our work contributes to this liquid sculpting process by providing a theoretical tool to predict the rate the liquid wets the dry pattern. Another intriguing finding of this work is that one can drastically vary the thickness of the films (into either fringe or bulk film) by controlling the hydrostatic pressure or the lane width.

ACKNOWLEDGMENTS

This work was supported by the National Research Foundation (Grant No. 2018-052541) and the Ministry of Trade, Industry and Energy (Grant No. 2018-20000187) of Korea via SNU-IAMD.

[1] D. Quéré, Wetting and roughness, Annu. Rev. Mater. Res. **38**, 71 (2008).
[2] J. Kim, M.-W. Moon, and H.-Y. Kim, Dynamics of hemiwicking, J. Fluid Mech. **800**, 57 (2016).
[3] L. Courbin, E. Denieul, E. Dressaire, M. Roper, A. Ajdari, and H. A. Stone, Imbibition by polygonal spreading on microdecorated surfaces, Nat. Mater. **6**, 661 (2007).
[4] J. Kim, M.-W. Moon, K.-R. Lee, L. Mahadevan, and H.-Y. Kim, Hydrodynamics of Writing with Ink, Phys. Rev. Lett. **107**, 264501 (2011).
[5] A. Russo, B. Y. Ahn, J. J. Adams, E. B. Duoss, T. Jennifer, and J. A. Lewis, Pen-on-paper flexible electronics, Adv. Mater. **23**, 3426 (2011).
[6] Y. Ito, Surface micropatterning to regulate cell functions, Biomaterials **20**, 2333 (1999).
[7] F. L. Geyer, E. Ueda, U. Liebel, N. Grau, and P. A. Levkin, Superhydrophobic–superhydrophilic micropatterning: Towards genome-on-a-chip cell microarrays, Angew. Chem., Int. Ed. **50**, 8424 (2011).
[8] L. Zhai, M. C. Berg, F. Ç. Cebeci, Y. Kim, J. M. Milwid, M. F. Rubner, and R. E. Cohen, Patterned superhydrophobic surfaces: Toward a synthetic mimic of the Namib Desert beetle, Nano Lett. **6**, 1213 (2006).
[9] A. Lee, M.-W. Moon, H. Lim, W.-D. Kim, and H.-Y. Kim, Water harvest via dewing, Langmuir **28**, 10183 (2012).
[10] H. Bai, L. Wang, J. Ju, R. Sun, Y. Zheng, and L. Jiang, Efficient water collection on integrative bioinspired surfaces with star-shaped wettability patterns, Adv. Mater. **26**, 5025-5030 (2014).
[11] D. E. Kataoka and S. M. Troian, Patterning liquid flow on the microscopic scales, Nature (London) **402**, 794 (1999).
[12] A. A. Darhuber, J. M. Davis, S. M. Troian, and W. W. Reisner, Thermocapillary actuation of liquid flow on chemically patterned surface, Phys. Fluids **15**, 1295 (2003).
[13] M. Lee, Y. S. Chang, and H.-Y. Kim, Drop impact on microwetting patterned surfaces, Phys. Fluids **22**, 072101 (2010).
[14] S. Kim, M.-W. Moon, and H.-Y. Kim, Drop impact on super-wettability-contrast annular patterns, J. Fluid Mech. **730**, 328 (2013).
[15] K.-H. Chu, R. Xiao, and E. N. Wang, Uni-directional liquid spreading on asymmetric nanostructured surfaces, Nat. Mater. **9**, 413 (2010).
[16] J. Li, X. Zhou, J. Li, L. Che, J. Yao, G. McHale, M. K. Chaudhury, and Z. Wang, Topological liquid diode, Sci. Adv. **3**, eaao3530 (2017).
[17] T.-G. Cha, J. W. Yi, M.-W. Moon, K.-R. Lee, and H.-Y. Kim, Nanoscale patterning of microtextured surfaces to control superhydrophobic robustness, Langmuir **26**, 8319 (2010).
[18] P. Eaton and P. West, *Atomic Force Microscopy* (Oxford University, Oxford, 2010).
[19] J. Jurin, An account of some experiments shown before the Royal Society; with an enquiry into the cause of the ascent and suspension of water in capillary tubes, Philos. Trans. R. Soc. London **30**, 739 (1718).

[20] See Supplemental Material at http://link.aps.org/supplemental/10.1103/PhysRevFluids.6.034002 for videos S1–S6.
[21] S. J. Kim, M.-W. Moon, K.-R. Lee, D.-Y. Lee, Y. S. Chang, and H.-Y. Kim, Liquid spreading on superhydrophilic micropillar arrays, J. Fluid Mech. **680**, 477 (2011).
[22] F. Brochard-Wyart, G. Debrégeas, and P. G. de Gennes, Spreading of viscous droplets on a non viscous liquid, Colloid Polym. Sci. **274**, 70 (1996).
[23] J. Kim, M.-W. Moon, and H.-Y. Kim, Capillary rise in superhydrophilic rough channels, Phys. Fluids **32**, 032105 (2020).
[24] B. Levich and L. Landau, Dragging of a liquid by a moving plate, Acta Physicochim. URSS **17**, 42 (1942).
[25] B. Levich, *Physicochemical Hydrodynamics* (Prentice Hall, New York, 1962).
[26] L. Fabié and T. Ondarçuhu, Writing with liquid using a nanodispenser: Spreading dynamics at the sub-micron scale, Soft Matter **8**, 4995 (2012).
[27] H.-Y. Kim, On thermocapillary propulsion of microliquid slug, Nanoscale Microscale Thermophys. Eng. **11**, 351 (2007).
[28] A. A. Darhuber, S. M. Troian, and W. W. Reisner, Dynamics of capillary spreading along hydrophilic microstripes, Phys. Rev. E **64**, 031603 (2001).